Research Article Vol. 3, No. 3 / 25 June 2025 / Optica Quantum 303

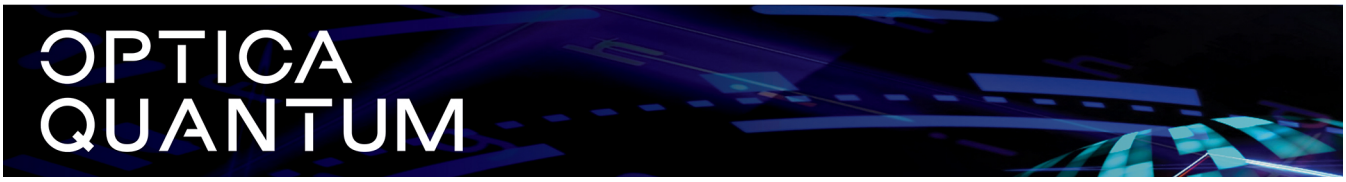

Noise impact of classical headers on the quantum payload in quantum wrapper networking

Gamze Gül,[1,2,*] Gregory S. Kanter,[2] Shannon G. Tan,[2] Mehmet Berkay On,[3] Roberto Proietti,[4] S. J. Ben Yoo,[3] and Prem Kumar[1,2,5]

[1]Graduate Program in Applied Physics, Northwestern University, Evanston, Illinois 60208, USA
[2]Center for Photonic Communication and Computing, Department of Electrical and Computer Engineering, Northwestern University, Evanston, Illinois 60208, USA
[3]Department of Electrical and Computer Engineering, University of California, Davis, Davis, California 95616, USA
[4]Department of Electronics and Telecommunications Engineering, Politecnico di Torino, Italy
[5]kumarp@northwestern.edu
*gamzegul@u.northwestern.edu

Received 31 January 2025; revised 20 May 2025; accepted 23 May 2025; published 25 June 2025

The fundamental properties of quantum mechanics, such as the no-cloning theorem, make management and control of quantum networks challenging. Quantum wrapper networking (QWN) offers a solution to this problem by wrapping quantum payloads with classical bits (as headers and/or tails) that can be used to assist with networking, performance monitoring, and probing the properties of the fiber interconnection. Since the classical header and quantum payload travel in the same fiber, one should carefully design the system to mitigate potentially deleterious effects such as noise and cross-talk. In this paper, we identify and characterize the noise induced by the classical headers by in-fiber scattering processes. We study the noise by using a tunable continuous-wave laser to emulate O-band (~1310 nm) classical headers, which are time- and wavelength-multiplexed with O-band quantum signals. The noise is characterized as a function of the headers' power, classical-quantum wavelength detuning, and optical fiber length. We demonstrate that the dominant noise contribution originates from spontaneous Raman scattering for wavelength detunings that are larger than 3 nm. We also observe that some noise photons can bleed into the quantum payload due to Rayleigh scattering of backward Raman scattered photons. We further investigate system level impacts of the noise created by classical headers that are produced by employing a small form-factor pluggable transceiver. We demonstrate that the associated noise level has negligible impact on quantum payloads for a 47.8 km deployed fiber link, the longest length used in QWN experiments to date, achieving a coincidences-to-accidentals ratio of 56 and a two-photon interference visibility of 88.8%.

https://doi.org/10.1364/OPTICAQ.558540

1. INTRODUCTION

Functional large scale quantum networks will allow quantum resources to be shared between numerous remote users to realize applications that classical systems cannot offer, such as quantum teleportation and distributed quantum computing [1–3]. Quantum networking research has seen rapid growth in the past years, showing advancement in quantum metropolitan area fiber optic infrastructures [4–10], transnational links [6,11], and even a backbone network connecting multiple metropolitan networks with the integration of satellite-to-ground links [12]. However, for larger quantum networks to operate seamlessly, there needs to be a universal protocol to connect quantum nodes. What makes this particularly challenging for quantum systems is that, unlike classical communication traffic, quantum information cannot be monitored or tapped without destroying qubits. Furthermore, this protocol needs to allow scalability, interoperability, and coexistence with classical networks while preserving the integrity of quantum information.

Quantum wrapper networking (QWN) technology [13] is an emerging candidate to address these challenges. QWN offers a solution for the end-to-end transport of quantum information (quantum payload) by wrapping it with classical information (QW headers and QW tails) and using them for switching and routing. By adopting classical networking protocols and employing low-loss classical devices, the transmission of quantum information to its destination can be achieved while monitoring the classical headers to infer information about the quantum signal such as polarization drift and loss. QWN also aims to use QW headers for time synchronization which was previously demonstrated by wavelength multiplexing classical pulses to coexist with quantum signals in quantum networks [14]. Initial experiments havve also shown packet switching polarization entangled single-photon payloads to two distinct nodes while monitoring the loss performance in the network [15]. Similarly, [16] proposed packet switching of quantum key distribution (QKD) signals using classical headers for networked systems.

The wavelength chosen for the quantum payloads and classical headers reveals a trade-off between noise and loss in the quantum channel and the degree of flexibility/scalability that headers can offer. In general, placing quantum and classical information (QWN headers or coexisting classical traffic) as far away as possible in wavelength from the quantum channel reduces the noise since the spontaneous Raman scattering (SpRS) coefficient tends to be lower for larger wavelength detunings [17]. Indeed, in coexisting scenarios, quantum and classical data channels are usually placed in different telecommunications bands [mostly O-band (1260–1360 nm) and C-band (1530–1565 nm) or L-band (1565–1625 nm)] [18,19]. However, large wavelength separations between headers and the quantum payload for QWN reduces the benefits of co-propagating headers since they cannot effectively be used to monitor and track the quantum signal for wavelength-dependent effects such as phase and polarization drift [20,21]. Time multiplexing quantum and classical communication channels is an option for coexisting scenarios to have both channels on the same band [22]. In addition to having classical communication traffic, time multiplexed classical signals can act as a reference signal to align the systems to track phase [20] and polarization fluctuations [4,21]. Depending on the wavelength, optical power, duration of the quantum and classical payloads in the time-multiplexed scenario, and the optical properties of the fiber channel, the number of noise photons and their impact on the quantum signal vary.

Therefore, it is crucial to characterize and identify the noise impact on quantum payloads by the classical signals around it and design the QW datagrams accordingly. In this paper, we study the noise components of our time- and wavelength-multiplexed QWN implementation for O-band quantum payloads by using a continuous-wave (CW) laser to emulate O-band QW headers. The noise is characterized as a function of the headers' power, classical-quantum wavelength detuning, and optical fiber length. We show that the strongest noise contribution comes from backscattered spontaneous Raman scattering (SpRS) of the headers that is Rayleigh rescattered in the forward direction. Using headers with a peak power of approximately −8 dBm, over fiber lengths up to 50 km, we show that this noise contribution is negligible. We further verify noise tolerance by generating QW headers using a small form-factor pluggable (SFP) transceiver and propagating quantum datagrams in a metropolitan scale deployed fiber-optic link of 47.8 km between Evanston and Chicago by achieving a coincidences-to-accidentals-coincidence ratio (CAR) of 56 and a two-photon interference visibility of 88.8%.

2. QUANTUM WRAPPER DATAGRAMS

In quantum wrapper networking, the quantum payload and classical QW headers (and optionally QW tails) travel in the same fiber. The header can contain necessary networking information such as the source ID, destination ID, quantum payload duration, quantum data type, and extra bits to perform error estimation. The header optical power and polarization state provide additional parameters for observing channel quality and provide information to the network nodes, specifically to edge quantum wrapper switch routers (QWSRs) which unwrap QW datagrams and process the headers to use them for timing purposes such as clock recovery and synchronization. In this way, QWN allows users to make measurements on the QW headers and tails, detect the impairments that degrade the channel quality, and infer the potential impacts on the quantum payload. Unfortunately, if not managed properly, noise photons created by the header and tail signal itself can overlap with and degrade the quantum payload. The quantity of noise photons can be negligible or substantial, depending on the wavelength, optical power, and duration of the header. In addition, the quantum payload duration, quantum application, traffic in the QW network (both coexisting QW datagrams and classical communication signals), and the available quantum transmitter and receiver technologies at the QWN nodes impact the noise characteristics.

One can prepare the QW datagrams by generating the classical bits and quantum payload, and multiplex them at the edge QWSR as shown in Fig. 1. After they arrive at their destination (a label indicating the destination node is contained in the QW datagram), the quantum payload and the wrapper bits are demultiplexed at the edge QWSR. Both wavelength- and time-multiplexing can be performed depending on the wavelength selection. In our paper, we employed a switch to achieve both wavelength- and time-multiplexing at the source and used cascaded dense wavelength division multiplexing (DWDM) multiplexers to demultiplex the signals at the destination. We chose a wavelength spacing of 3.3 nm between the classical header and quantum payload, which is large enough to allow for easy separation through filtering, but close enough to preserve tight arrival time variation and polarization correlations [23]. In Section 3.2, classical headers were generated by using an SFP, which is a convenient choice that we employ as a low-cost, low-performance example of how to realize QW datagrams. More details about the wrapper bit generation and potential improvements can be found in Appendix A. Our intention is to test a QWN protocol that judiciously chooses channel separation in time and wavelength to balance the advantages of noise tolerance against those of signal monitoring capability.

3. RESULTS

3.1. Investigation of the Noise

Because the classical header and quantum payload in our protocol are time- and wavelength-division multiplexed, the only way that noise from the header can corrupt the quantum signal in our system is through a nonlinear process (to get into the same frequency band as the payload) plus one or more scattering processes (to get into the same time window as the payload). In a single-mode fiber employed in a fiber network, classical headers can generate nonlinear noise photons through spontaneous Raman scattering (backward and forward), Brillouin scattering, and four-wave mixing (FWM). Rayleigh and double-Rayleigh scattering, however, are the secondary linear scattering processes that can temporally shift nonlinear generated noise into the quantum payload's time window.

Due to system design, we can immediately eliminate Brillouin scattering as a nonlinear mechanism for noise generation since potential Brillouin scattering from headers is too narrowband to affect the quantum payload. As shown in Fig. 1, our protocol uses a ∼3-nm wavelength division separation between the headers and quantum payload, and Brillouin gain frequency shift and bandwidth for single-mode fibers are of the order of 10–20 GHz and 50–100 MHz, respectively [24,25]. Therefore, Brillouin noise is easily filtered out by the DWDM filters employed. This leaves spontaneous Raman scattering and four-wave mixing as the potential culprits for nonlinear noise generation. We devised

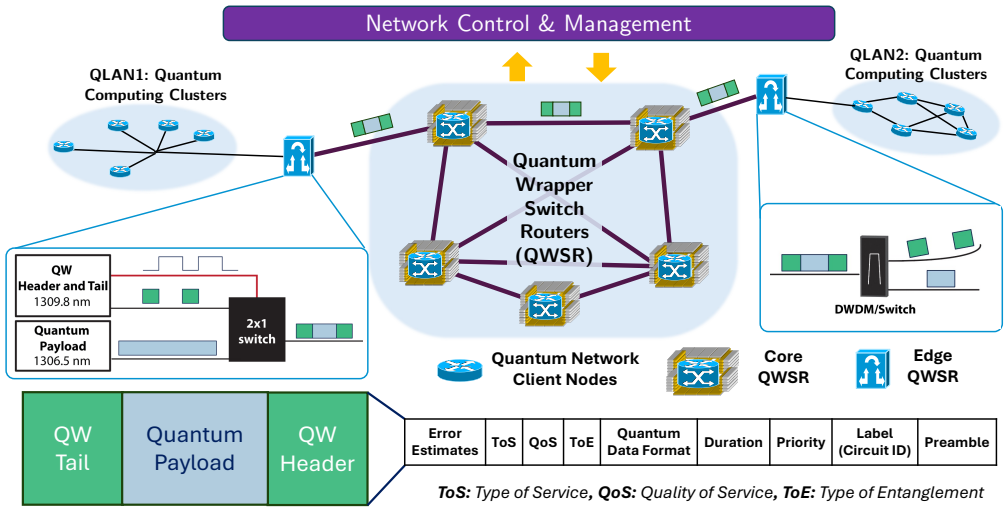

Fig. 1. QWN networking architecture that connects local area quantum networks with edge and core quantum wrapper switch routers. An example edge QWSR consists of a switch to wrap quantum payload from the quantum network client node. Quantum wrapper datagrams consist of classical headers (optionally tails) which carry information about the quantum payload duration, type of entanglement (ToE), the source ID, the destination ID, quality of service (QoS), and bits to estimate and correct errors.

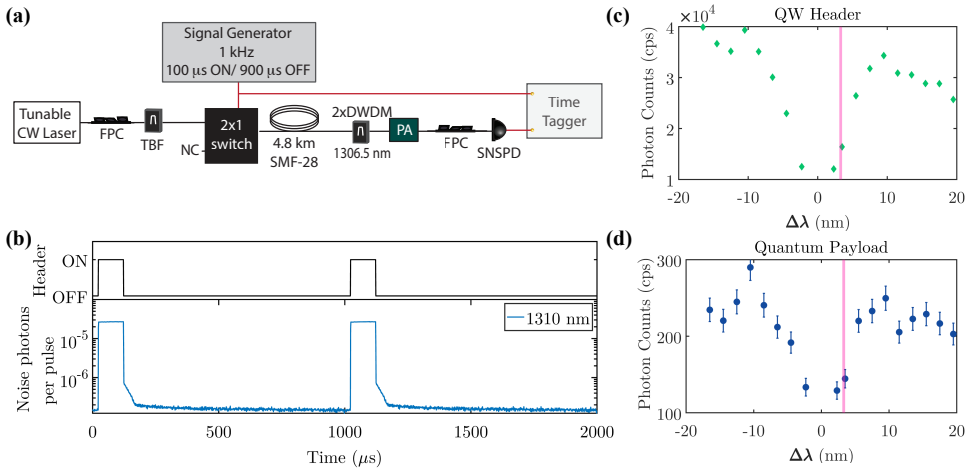

Fig. 2. (a) Experimental setup to measure noise photons. FPC, fiber polarization controller; TBF, tunable bandpass filter; NC, not connected; PA, free-space polarization analyzer. (b) Noise photons in the time domain. (c) Noise photons in the header time span (100 μs) as a function of the wavelength of the tunable CW laser recorded for 1 s. (d) Noise photons in the quantum payload time span (900 μs) as a function of the wavelength of the tunable CW laser recorded for 1 s. Noise photons for the wavelength detuning (3.3 nm) between the QW header and the quantum payload used in the deployed fiber experiments are highlighted with the pink bands in Figs. 2(c) and 2(d).

a setup, Fig. 2(a), to look at nonlinear power dependence, nonlinear gain bandwidth, and fiber length dependence to determine noise contributions of each nonlinear processes in the quantum payload. A 2×1 switch shown in Fig. 1 interleaves the quantum payload and classical headers to form QWN datagrams. A tunable continuous-wave laser emulates the headers and varies the wavelength and power. This produces tunable "headers" (pumps) with a duration of 100 μs and a repetition rate of 1 kHz. We then use various lengths of fiber spools to experimentally characterize the noise photons in the time and frequency domains. Here, we leave the quantum payload port of the switch unconnected ("NC" in Fig. 2) and measure the single-photon counts in the quantum payload wavelength-band centered at 1306.5 nm (filtered by two cascaded DWDMs, each with an extinction ratio of 40 dB bandwidth of 0.25 nm) so that only noise photons of interest are detected. The time tagger measures these photons in relation to the generated QW headers when it receives a signal of 1 kHz which is the same electrical signal that drives the switch.

In our first noise characterization experiment, we measure the nonlinear gain bandwidth of header-induced noise by inputting headers with a power of −8.4 dBm (−18.4 dBm average power due to the duty cycle) into a 4.8-km SMF-28 fiber spool and measure the noise photon counts with a superconducting nanowire single-photon detector (SNSPD) as we tune the wavelength of the CW laser. Figure 2(b) shows the ideal switching signal as a function of time (top) and noise photons generated in the quantum payload passband when the header is centered at 1310 nm (bottom). As expected, the photon counts outside the header are very small, but do not go to zero since the extinction ratio of the switch is limited to approximately 23 dB. In

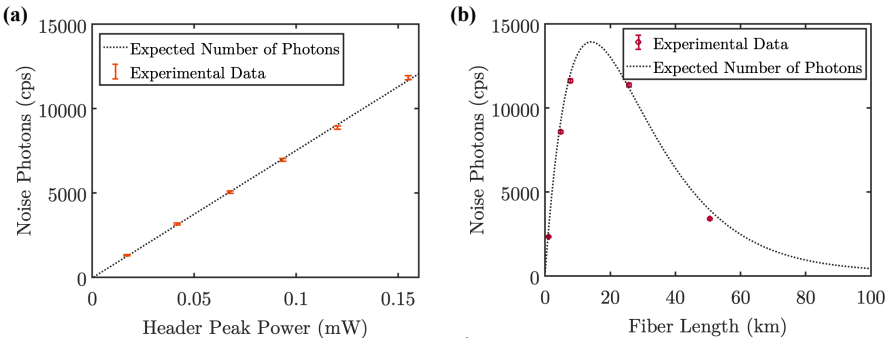

Fig. 3. (a) Linear dependence of the number of noise photons during header on the header peak power. (b) Comparison between the expected number of SpRS photons during the header timespan for different fiber lengths.

addition, an enhanced amount of header-generated noise bleeds into the quantum payload timespan during a ~50 μs transition time after the switch turns the header power off. Figures 2(c) and 2(d) show noise generation in the quantum payload passband as a function of header/pump wavelength detuning for header and quantum payload time windows, respectively. Note that we make sure to only tune pump headers to wavelengths outside of the payload passband to avoid collection of any pump photons. The pink bands in Figs. 2(c) and 2(d) show the noise photons for the wavelength detuning (3.3 nm) between the QW header and the quantum payload, which is the band employed in our QWN protocol described in Section 3.2. The wavelength dependence of the photons in the header [Fig. 2(c)] and quantum payload [Fig. 2(d)] time span demonstrates strong characteristics of SpRS gain spectra [17,26]. The photons detected during the payload time consist of the detector dark counts (~100 cps) and noise photons at that optical power, which are ~23 dB lower than the noise when the header is ON. We reduce the latter contribution in the subsequent QWN experiments by also turning off the laser that generates the headers during the quantum payload, thereby increasing the effective extinction ratio.

To verify that the nonlinear noise making it into the payload frequency passband and time span is indeed SpRS, we investigate the functional dependence of nonlinear photon generation versus header/pump peak power. For example, nonlinear noise generated by SpRS should linearly increase as a function of optical power, whereas FWM generated photons will be proportional to the square of the optical power. Figure 3(a) shows the noise photon counts detected during the header duration as we increased the header peak power. To carefully determine the functional dependence, a second-order polynomial function ($f(x) = ax^2 + bx + c$) was fitted to the experimental data in Fig. 3(a). The contribution of the second-order term was more than 10^3 times lower than the first-order term at these power levels, showing a strong linear dependence and negligible second-order dependence. This rules out any significant noise contribution of FWM for the power levels tested and shows the dominant noise contribution is most likely from SpRS.

As another verification of SpRS as the dominant header-induced noise source, we checked the noise dependence on the fiber length against the theoretical prediction of SpRS generation and fiber-induced loss described by

$$n_{\mathrm{H}}(P_0, L, \Delta\lambda) = n_{\text{f-SpRS}} + n_{\mathrm{d}} = \frac{P_0 G(\Delta\lambda)}{E_V} L e^{-\alpha L} \Delta\nu l \eta + n_{\mathrm{d}}. \quad \textbf{(1)}$$

Figure 3(b) shows noise photon counts during the header duration for five different fiber spools tested in the lab with the theoretically predicted SpRS counts from Eq. (1) overlayed.

Here, the SpRS coefficient ($G(\Delta\lambda)$) was obtained from the previous experiments shown in Figs. 2(c) and 2(d), P_0 is the average power of classical headers, E_V is the photon energy, l is the loss before the photons are detected, $\Delta\nu$ is the bandwidth of the cascaded DWDMs, η is the detector efficiency (87%), and n_d are measured detector dark counts. We calculated the effective length of a fiber spool as $Le^{\alpha L}$, where α is the loss for a single-mode fiber (SMF-28™); while the fiber spools have slightly different loss coefficients, we used $\alpha = 0.3$ dB/km as a typical average value. The close match between experimental data and predicted SpRS counts further verifies the dominant noise contribution is indeed SpRS. Note that even though we place both quantum and classical channels in the O-band, QWN in which both channels are in the C-band would have similar noise characteristics since SpRS is primarily a function of wavelength detuning [27].

Finally, to fully quantify the noise contribution during the payload, we need to verify the linear scattering mechanism of SpRS photons. Here, we compared the noise photon counts in the time-domain generated from fiber propagating headers from a CW laser (at a power of −8.4 dBm) with attenuated headers through different fiber spool lengths, see Figs. 4(a)–4(c). The wavelength of the attenuated classical header is chosen at the quantum payload's wavelength (1306.5 nm) to match with the DWDMs' passband and its power is adjusted to match with the peak photon count rates as the noise photons. This allowed us to differentiate the effects from the switch's extinction ratio (~23 dB) and that of scattered SpRS photons.

The number of noise photons in the quantum payload depends on the amplitude of the classical signal, the length of the fiber, and the extinction ratio of the switch. We observe this both on the attenuated signal and the noise photons due to the SpRS. However, after the header ends, we observe more counts in the noise photons compared with the attenuated signal. This showed that there are photons detected with a delay in the case of SpRS. The difference also depends on the fiber length. In 1-km and 4.8-km fiber spools, we observe these noise photons disappear around 10 and 46 μs after the end of the header, respectively, which correspond to the round-trip propagation times of the corresponding fibers. This effect can be explained by back-scattered SpRS generated during the header that is subsequently Rayleigh rescattered in the forward direction. A similar double scattering process of noise photons has been observed in

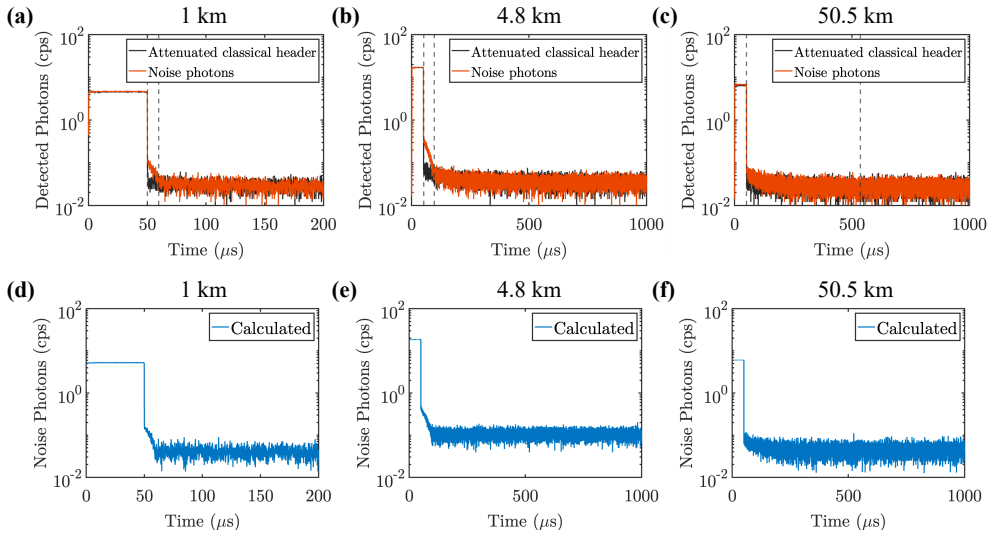

Fig. 4. Attenuated classical headers with a wavelength of 1306.5 nm (black) compared with the noise created by the 50 μs classical headers (orange) in SMF-28^{TM} fiber spools with the lengths of: (a) 1 km; (b) 4.8 km; and (c) 50.5 km. Calculated noise photons (blue) for the optical fibers with the lengths of: (d) 1 km; (e) 4.8 km; and (f) 50.5 km.

twin-field QKD over 500 km of fiber due to classical reference signals [20], though double Rayleigh scattering was the culprit. Noise from double Rayleigh scattering was also characterized for Raman amplifiers' performance [28,29]. In addition, the backward Rayleigh scattering of FWM noise was studied in [30] for core and wavelength allocation in QKD in multi-core fibers. In our system, the delay induced by Rayleigh-scattered, backscattered SpRS photons depends on when the scattering processes occur in the fiber, which cannot be longer than the round-trip propagation time. We can calculate the number of noise photons during the quantum payload duration by

$$n_{\mathrm{QP}}(P_0, L, \Delta\lambda) = n_{\text{b-SpRS-Rayleigh}} + n_{\text{f-SpRS}} + n_{\mathrm{d}}, \tag{2}$$

where

$$n_{\text{b-SpRS-Rayleigh}} = \frac{P_0 S G(\Delta\lambda)}{2E_V\alpha} e^{-\alpha L}[L + \frac{e^{-2\alpha L}}{2\alpha} - \frac{1}{2\alpha}]\Delta\nu l\eta \tag{3}$$

and

$$n_{\text{f-SpRS}} = C_{\mathrm{ER}} \frac{P_0 G(\Delta\lambda)}{E_V} L e^{-\alpha L}\Delta\nu l\eta. \tag{4}$$

Here, the first term represents the Rayleigh scattering of backscattered SpRS photons with random polarization, the second term is the forward Raman scattering of the header, and the third represents the detector dark counts. Equation (3) is based on the double Rayleigh scattering study in [31]. However, our derivation starts with the backward SpRS. The parameter S in Eq. (3) is the Rayleigh scattering coefficient and C_{ER} in Eq. (4) represents the total extinction ratio of the header (e.g., for a CW laser, the extinction ratio of the header is just the extinction ratio of the switch). When we encode information with a field programmable gate array (FPGA) board and generate the classical headers with an SFP module such as in our deployed fiber tests in Section 3.2, the header transmitter's laser is disabled through FPGA logic. Therefore, there is no optical power to generate forward SpRS during the quantum payload (very high extinction ratio). Figures 4(d)–4(f) show the predicted noise photons during the payload using Eq. (3) for the same fiber lengths in Figs. 4(a)–4(c). More details about the calculations can be found in Appendix B.

In the 50.5-km fiber spool, Figs. 4(c) and 4(f), the rescattered photons are no longer differentiable from the other noise photons (forward SpRS and the dark counts), as in the shorter fibers tested, since fiber loss for a roundtrip propagation length dominates over SpRS. Therefore, rescattered SpRS noise, the dominant header-induced noise contribution in the quantum payload for the O-band/O-band QWN protocol investigated here, is likely insignificant for long fiber lengths.

3.2. Noise Impact of Header on Quantum Payload in Deployed Fibers

Although the characterization of the noise showed that the bulk of noise photons generated by headers stay in the classical header timespan, and those during the quantum payload are not substantial, we sought to verify this in deployed fiber for a metropolitan scale network. For this test, we sent QW datagrams in a 47.8 km deployed fiber link between our lab at Northwestern University and Starlight in Chicago, see Fig 5. The total link loss including the loss due to the fiber length, connectors, and the insertion loss of the switch at the Chicago location (<1.5 dB) is 19 dB. The headers are prepared by the methods described in Appendix A. Although we did not analyze the received headers in this experiment, we refer the reader to Ref. [15] for an extensive study of SFP-based header generation and detection for QWN.

Our polarization entangled photon pair source generates entangled photon pairs in a Bell state $|\Psi\rangle = \frac{1}{\sqrt{2}}(|HH\rangle + |VV\rangle)$ with 97.9±0.4% fidelity [32]. The signal photons of the polarization entangled photon pairs were wrapped by the QW headers and sent over the Chicago fiber link while the idler photons were detected without transmission through the network.

We performed coincidence count (CC) measurements to study the quality of this transmission, as shown in Fig. 6. The coincidence counts histograms show the number of coincidence counts as a function of delay between the detection of signal and idler photons at the receiver at Northwestern. Ideally, these histograms should have a peak at 0 (assuming the delay due to fiber length difference is adjusted for in the post processing) showing the true coincidence counts of the

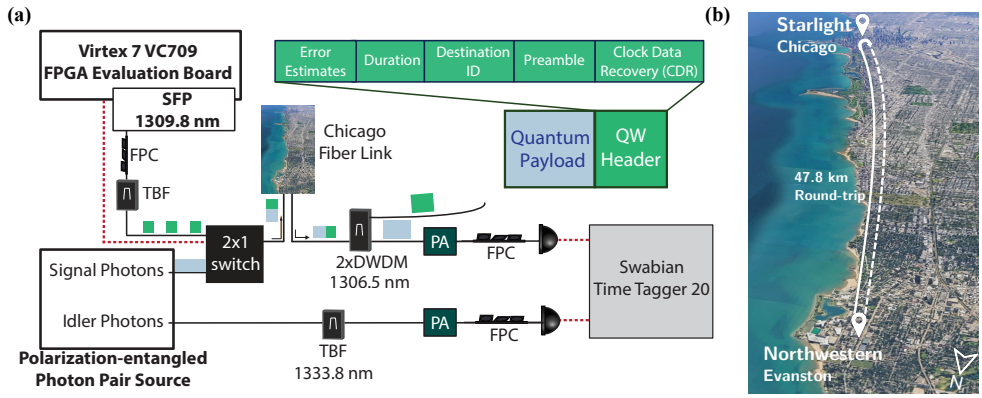

Fig. 5. (a) Experimental setup to create the QW headers, and building the QW datagrams for the signal photons of polarization entangled photon source. (b) The map of the the deployed fiber link locations.

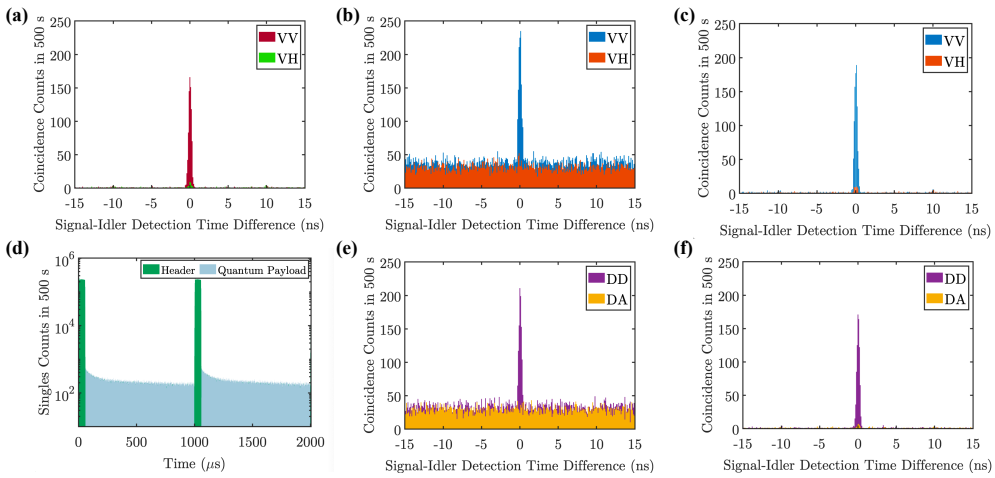

Fig. 6. Coincidence count histograms for idler and signal photons.The bin width of the histograms is 100 ps. Idler photons are detected directly following generation. (a) Signal photons travel in 47.8 km deployed fiber without QW headers. (b) and (e) Signal photons travel in 47.8 km deployed fiber with QW headers. (c) and (f) Signal photons travel in 47.8 km deployed fiber with QW headers but real-time temporal gating via the time tagger eliminates the photons detected during the header timespan. (d) Singles counts of the signal and the noise photons.

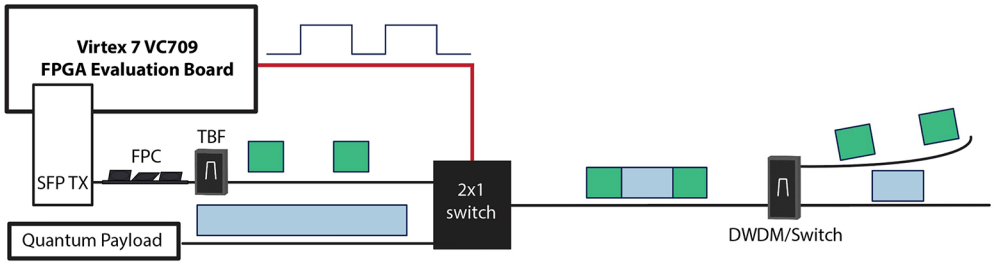

Fig. 7. Experimental setup to create and multiplex classical headers. FPC, fiber polarization controller; DWDM, dense wavelength division multiplexing; TBF, tunable bandpass filter; SFP TX, small-form factor pluggable transceiver.

signal and idler. However, due to the noise in the systems, we also detect accidental coincidence counts (ACC). We use the CAR for the quality of transmission, calculated by CAR = (CC−ACC)/ACC, and the visibility of entangled photons, given by V = $(CC_{VV}-CC_{VH})/(CC_{VV}+CC_{VH})$, in horizontal and vertical basis (DD and DA for diagonal/antidiagonal basis).

Figure 6(a) shows the coincidence count histograms for signal and idler photons if there is no QW header to wrap them. Without the noise created by the headers, the CAR and the visibility in HV basis are 77 and 91.7±2.6%, respectively, for a coincidence window of 1.2 ns. The error in the visibility is calculated as 2 standard deviations based on photon counting statistics. Figures 6(b) and 6(e) show the coincidence counts when the noise photons from QW headers are also detected, resulting in a CAR of less than 4, which means the noise

photons created during the QW header timespan cause accidental coincidences with the idler photons detected in the other SNSPD. Since we know that the majority of the noise is created during the header timespan, we can apply a time filtering during the data acquisition. For this work, we used the Swabian time tagger's virtual channel property to time filter (temporal gate) the detected photons to post select the detections only occurring during the quantum payload [33]. In other words, we only looked at the coincidence counts between the detections during quantum payload and idler photons. These detections include the noise photons due to backward-SpRS-Rayleigh scattering, signal photons, and the detector dark counts, as shown in the blue region in Fig. 6(d). This method eliminated the accidental coincidence counts due to the noise in the header timespan, giving a CAR of 56 (64) and 88.8±2.9% (92.3±2.6%) visibility in HV (DA) basis. This performance shows negligible degradation compared with transmission without QW headers. Here, the imperfect visibility of 88.8% comes mainly from slight system misalignment rather than header-generated noise. This indicates that our QWN protocol using time- and wavelength-division multiplexing for O-band/O-band headers/payload has a high noise tolerance for fiber transmission in the presence of classical headers in deployed fiber scenarios.

4. CONCLUSION

In this work, we investigated the noise tolerance of a QWN protocol where classical headers and the quantum payload were time- and wavelength division multiplexed, at close wavelength separation, to simultaneously allow for noise isolation and the potential for quantum payload monitoring and tracking.

In a detailed noise characterization, we observed that the extinction ratio of the switch to create headers had an impact on the noise photons during the quantum payload time span. However, we fixed this in the deployed fiber experiments by using an SFP and turning it ON and OFF through the FPGA logic. We found that the dominant contribution of noise to the quantum payload from the classical signal headers is due to Rayleigh backscattering of Raman scattered photons in the backward direction.

This contribution was measured to be less than 0.1 photon per quantum payload for a QW datagram consisting of 940 μs quantum payload and 60 μs classical header of −8.4 dBm power. To further verify that this noise was negligible, we examined the CAR and visibility of a polarization-entangled payload through 47.8 km of deployed fiber in the Chicago area, obtaining values of 56 and 88.8%, respectively.

Our results show the QWN protocol is worth investigating further to test the ability of headers for quantum payload monitoring and tracking, particularly compensation of polarization fluctuation and drift. In addition, the high noise tolerance of our O-band/O-band protocol shows promise of successful coexistence of classical data traffic in the C-band. We note that our system needs to be analyzed further by fully characterizing the effect of this noise with more sophisticated quantum measurements such as quantum state tomography. We are also aware that the current system relies on the high extinction ratio of the DWDMs which have a fixed bandwidth and central wavelength. Wavelength detunings less than 3 nm can reveal other noise contributions with double Rayleigh and Brillouin–Rayleigh scattering combinations. However, the calculations demonstrated here can be used by replacing or adding the other noise factors in the system. The robustness of our protocol for O-band quantum payloads with O-band classical headers is a promising step in the advancement of QWN toward practical quantum networking.

APPENDIX A: PREPARATION OF QUANTUM WRAPPER HEADERS

A detailed explanation of the quantum wrapper header transceiver for QWNs may be found in [15]. For our experiments, we use a simpler design for the transceiver. The quantum wrapper headers (QW headers) implemented in our experimental setup are composed of burst-mode classical optical transmissions at a speed of 10 Gb/s and a O-band wavelength of 1309.8 nm. To create the data in the headers, as shown in Fig. 7, we used a Xilinx Virtex-7 VC709 FPGA board to generate the electrical header signals with the onboard transceiver cores. These electrical signals were then converted to optical QW headers using a 40 km 10 Gb/s SFP transceiver. To account for the quantum payload transmission period, we turned off the SFP laser during the payload transmission. This was done in FPGA logic using the TX_DISABLE pin of the SFP, and is user adjustable to account for different payload lengths. As such, the length in time of the header was approximately 60 μs and the length of the payload was adjusted to 940 μs.

An important thing to note regarding the header transceivers is that the transmission and reception of the header was done on the same VC709 FPGA board with the same SFP. This meant that the TX and RX shared a clock (156.25 MHz), which permitted a much simpler alignment process when receiving the data. This contrasts with clock and data recovery (CDR) done in [15], where, due to using multiple FPGA boards, a complex CDR method was used.

As such, the header is composed of a 41.8 μs CDR sequence, a start alignment frame, an 8-bit destination ID repeated eight times for redundancy (totaling another 64-bit frame), a 16-bit payload payload duration information repeated four times, and then a 2048-frame 11-bit pseudo-random binary sequence (PRBS) for bit error-rate checking. The last frame in the header is the stop frame, which is another 64-bit sequence for signaling the end of the frame. The majority of the payload consists of the PRBS sequence. In addition to the data, we added a guard time to account for the TX Laser power-on and power-off time. This guard time is adjustable, but was set to 16 μs for our setup.

To multiplex these header bits with the quantum payload, we used a fast 2×1 fiber-optic switch from Agiltron. This allows us to use any wavelength for the quantum wrapper header with any wavelength for the quantum payload without interference.

We acknowledge the technological limitations of our approach both in hardware and software. For example, a faster FPGA and optical transceiver bitrate could allow for a shorter header, thus increasing throughput. In addition to this, a more complex CDR scheme such as that done in [34] could significantly reduce the length of the CDR sequence, which currently is the longest section of the header. In addition to the throughput, adding error correction and encryption to the header could allow for a more secure and fault-tolerant transmission for sensitive applications.

Furthermore, any transceiver can be used to generate QW headers, and it remains an open research question to design a QW modulation and detection method. However, SFPs are a low-cost, low-performance method to realize QWN. The distance limits of SFPs (such as 40 km) are typically due to received

power limitations; therefore, those with an avalanche photodiode (APD) as a receiver can work over longer ranges, as in [35]. Note that there is little dispersion in a standard fiber in the O-band, so dispersion is not the limit. In these scenarios, the launch powers can additionally be attenuated if necessary.

One could also amplify the optical signal either at the transmitter or as a pre-amplifier to extend the range. SFPs are typically used for unamplified systems, primarily due to cost and convenience for mass-market applications; however, this does not have to be the case here. We should also note that the SFP received powers are specified for raw bit-error-rate (BER); therefore, by incorporating forward error correction (FEC), one can significantly improve the sensitivity. Using a Reed-Solomon-FEC (RS-FEC) (544:514) code alone provides more than 5 dB of operating margin at a less than 6% overhead [36].

In addition [37], demonstrates the potential advantage of even simple semiconductor optical amplifiers (SOAs) based optical amplification as a pre-amplifier for SFPs, which performs approximately 5 dB better than an APD. However, SFPs are inherently not high-performance devices, and future developments seem poised to lead to significant performance improvements, including even O-band coherent detection [38].

APPENDIX B: RAYLEIGH/RAMAN SCATTERING

The time and wavelength multiplexed classical headers in our quantum wrapper networking system undergo scattering in the optical fiber. These are Brillouin, Raman, and Rayleigh scatterings. In our experimental setup, we use a wavelength separation of 3.3 nm because we have DWDMs at 1306.5 nm and an SFP module at 1309.8 nm. This wavelength detuning eliminates the noise photons due to the leakage of the classical headers or scattered photons due to Rayleigh and Brillioun scattering, as explained in the main text. However, we still detect the Raman-scattered photons. Therefore, it is important to calculate the contribution of Raman-scattered photons as a function of header power, header duration, fiber length, and wavelength detuning.

We calculate the noise photons similar to the double-Rayleigh scattering analysis in [20]. In our cases, the strongest scattering process is the Raman scattering due to the wavelength multiplexing. As the classical header travels in the single-mode optical fiber with loss coefficient α and length L, Raman scattering occurs in both directions.

Assuming the Raman scattering occurred at L' as shown in Fig. 8, and the probability of backward and forward Raman scattering is the same, we would have the following equation for the Raman scattered optical power at $z = L'$:

$$dP_{Raman} = P_0 e^{-\alpha L'} G(\Delta\lambda)\Delta\nu dL'. \tag{B1}$$

The forward Raman scattering power at the end of the optical fiber ($z = L$) due to the Raman scattering at $z = L'$ after the fiber loss to the remaining length of $L - L'$ is

$$dP_{f-SpRS} = P_0 e^{-\alpha L'} G(\Delta\lambda)\Delta\nu e^{-\alpha(L-L')} dL'. \tag{B2}$$

The backward Raman scattering power at the beginning of the optical fiber ($z = 0$) due to the Raman scattering at $z = L'$ after the trip back to the beginning is

$$dP_{b-SpRS} = P_0 e^{-\alpha L'} G(\Delta\lambda)\Delta\nu e^{-\alpha L'} dz. \tag{B3}$$

The backward Raman scattered photons can scatter again in the opposite direction. If this happens at $z = L''$ with the Rayleigh

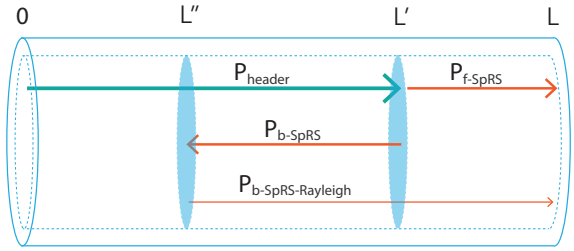

Fig. 8. Directions of the classical headers and scattering processes due to these headers in the single-mode fiber.

scattering coefficient of S, the power at the end of fiber due to this double scattering process is

$$\begin{aligned} dP_{b-SpRS-Rayleigh} &= P_0 e^{-\alpha L'} G(\Delta\lambda)\Delta\nu e^{-\alpha(L'-L'')} S e^{-\alpha(L-L'')} dL'' dL' \\ &= P_0 G(\Delta\lambda)\Delta\nu S e^{-\alpha L} e^{-2\alpha(L'-L'')} dL'' dL'. \end{aligned} \tag{B5}$$

Here, we are interested in both the number of noise photons generated at $z = L$ and the delay in their arrival time due to the extra trip in the fiber of $2(L' - L'')$.

The scattered power at $z = L$ due to the Rayleigh scattering of backward Raman scattered light is therefore,

$$\begin{aligned} P_{b-SpRS-Rayleigh} &= \int_0^L \int_0^{L'} P_0 G(\Delta\lambda)\Delta\nu S e^{-\alpha L} e^{-2\alpha(L'-L'')} dL'' dL' \\ &= P_0 G(\Delta\lambda)\Delta\nu S \frac{e^{-\alpha L}}{4\alpha^2}(2\alpha L + e^{-2\alpha L} - 1). \end{aligned} \tag{B6}$$

Funding. U.S. Department of Energy (DE-SC-0022336).

Acknowledgment. The authors would like to acknowledge the support of StarLight International/National Communications Exchange Facility. We also thank Kim Fook Lee from Northwestern University for the discussions during the design process of the polarization entanglement source and James van Howe from Augustana College for help in the editing process.

Disclosures. The authors declare no conflicts of interest.

Data availability. Data underlying the results presented in this paper are not publicly available at this time but may be obtained from the authors upon reasonable request.

REFERENCES

1. H. J. Kimble, "The quantum internet," Nature **453**, 1023–1030 (2008).
2. S. Wehner, D. Elkouss, and R. Hanson, "Quantum internet: A vision for the road ahead," Science **362**, eaam9288 (2018).
3. T. D. Ladd, F. Jelezko, R. Laflamme, *et al.*, "Quantum computers," Nature **464**, 45–53 (2010).
4. A. N. Craddock, A. Lazenby, G. B. Portmann, *et al.*, "Automated distribution of polarization-entangled photons using deployed New York City fibers," PRX Quantum **5**, 030330 (2024).
5. E. Bersin, M. Grein, M. Sutula, *et al.*, "Development of a Boston-area 50-km fiber quantum network testbed," Phys. Rev. Appl. **21**, 014024 (2024).
6. S. P. Neumann, A. Buchner, L. Bulla, *et al.*, "Continuous entanglement distribution over a transnational 248 km fiber link," Nat. Commun. **13**, 6134 (2022).
7. R. C. Berrevoets, T. Middelburg, R. F. Vermeulen, *et al.*, "Deployed measurement-device independent quantum key distribution and bell-state measurements coexisting with standard internet data and networking equipment," Commun. Phys. **5**, 186 (2022).
8. J. Dynes, A. Wonfor, W.-S. Tam, *et al.*, "Cambridge quantum network," npj Quantum Inf **5**, 101 (2019).

9. Y. Pelet, G. Sauder, M. Cohen, *et al.*, "Operational entanglement-based quantum key distribution over 50 km of field-deployed optical fibers," Phys. Rev. Appl. **20**, 044006 (2023).
10. M. Zahidy, D. Ribezzo, C. De Lazzari, *et al.*, "Practical high-dimensional quantum key distribution protocol over deployed multi-core fiber," Nat. Commun. **15**, 1651 (2024).
11. S. Wengerowsky, S. K. Joshi, F. Steinlechner, *et al.*, "Passively stable distribution of polarisation entanglement over 192 km of deployed optical fibre," npj Quantum Inf **6**, 5 (2020).
12. Y.-A. Chen, Q. Zhang, T.-Y. Chen, *et al.*, "An integrated space-to-ground quantum communication network over 4,600 kilometres," Nature **589**, 214–219 (2021).
13. S. J. Ben Yoo, S. K. Singh, M. B. On, *et al.*, "Quantum wrapper networking," IEEE Commun. Mag. **62**, 76–81 (2024).
14. I. A. Burenkov, A. Semionov, Hala, *et al.*, "Synchronization and coexistence in quantum networks," Opt. Express **31**, 11431–11446 (2023).
15. M. B. On, R. Proietti, G. Gül, *et al.*, "Experimental demonstration of datagram switching with monitoring in quantum wrapper networks," J. Lightwave Technol. **1**, 1–11 (2024).
16. R. Mandil, S. DiAdamo, B. Qi, *et al.*, "Quantum key distribution in a packet-switched network," npj Quantum Inf **9**, 85 (2023).
17. D. Hollenbeck and C. D. Cantrell, "Multiple-vibrational-mode model for fiber-optic Raman gain spectrum and response function," J. Opt. Soc. Am. B **19**, 2886–2892 (2002).
18. Y. Mao, B.-X. Wang, C. Zhao, *et al.*, "Integrating quantum key distribution with classical communications in backbone fiber network," Opt. Express **26**, 6010–6020 (2018).
19. J. M. Thomas, G. S. Kanter, and P. Kumar, "Designing noise-robust quantum networks coexisting in the classical fiber infrastructure," Opt. Express **31**, 43035–43047 (2023).
20. J.-P. Chen, C. Zhang, Y. Liu, *et al.*, "Sending-or-not-sending with independent lasers: Secure twin-field quantum key distribution over 509 km," Phys. Rev. Lett. **124**, 070501 (2020).
21. J. Chen, G. Wu, L. Xu, *et al.*, "Stable quantum key distribution with active polarization control based on time-division multiplexing," New J. Phys. **11**, 065004 (2009).
22. J. Wang, B. J. Rollick, Z. Jia, *et al.*, "Time-interleaving enabled co-propagation of QKD and classical channels over 100-km fiber with 10-dbm classical launch power," arXiv (2023).
23. G. Xavier, G. V. De Faria, G. Temporão, *et al.*, "Full polarization control for fiber optical quantum communication systems using polarization encoding," Opt. Express **16**, 1867–1873 (2008).
24. A. Kobyakov, M. Sauer, and D. Chowdhury, "Stimulated Brillouin scattering in optical fibers," Adv. Opt. Photonics **2**, 1–59 (2009).
25. Y. Koyamada, S. Sato, S. Nakamura, *et al.*, "Simulating and designing Brillouin gain spectrum in single-mode fibers," J. Lightwave Technol. **22**, 631–639 (2004).
26. C. Liang, K. F. Lee, M. Medic, *et al.*, "Characterization of fiber-generated entangled photon pairs with superconducting single-photon detectors," Opt. Express **15**, 1322–1327 (2007).
27. T. Ferreira da Silva, G. B. Xavier, G. P. Temporão, *et al.*, "Impact of Raman scattered noise from multiple telecom channels on fiber-optic quantum key distribution systems," J. Lightwave Technol. **32**, 2332–2339 (2014).
28. S. Lewis, S. Chernikov, and J. Taylor, "Characterization of double Rayleigh scatter noise in Raman amplifiers," IEEE Photonics Technol. Lett. **12**, 528–530 (2000).
29. Q. Feng, W. Li, and L. Huang, "Analysis of spontaneous Raman and Rayleigh scatterings in distributed fiber Raman amplification systems based on a random distribution model," IEEE Photonics J. **9**, 1–8 (2017).
30. W. Kong, Y. Sun, Y. Gao, *et al.*, "Core and wavelength allocation schemes for noise suppression in quantum key distribution over multicore fiber," IEEE J. Sel. Top. Quantum Electron. **29**, 1–12 (2022).
31. J.-P. Chen, C. Zhang, Y. Liu, *et al.*, "Supplemental material: Sending-or-not-sending with independent lasers: Secure twin-field quantum key distribution over 509 km," Phys. Rev. Lett. 124, 070501 (2020).
32. G. Gül, M. B. On, S. G. Tan, *et al.*, "Quantum wrapper networking: Investigating the noise impact of classical headers on the quantum payload," in *Frontiers in Optics + Laser Science 2024 (FiO, LS)* (Optica Publishing Group, 2024), p. FM3C.6.
33. *Time Tagger User Manual*. Swabian Instruments, May. 7, 2025. Accessed: May 18, 2025. [Online]. Available: https://www.swabianinstruments.com/static/documentation/TimeTagger/index.html.
34. R. Yu, R. Proietti, S. Yin, *et al.*, "10-Gb/s BM-CDR circuit with synchronous data output for optical networks," IEEE Photonics Technol. Lett. **25**, 508–511 (2013).
35. A. Rahmouni, P. Kuo, Y.-S. Li-Baboud, *et al.*, "100-km entanglement distribution with coexisting quantum and classical signals in a single fiber," J. Opt. Commun. Netw. **16**, 781–787 (2024).
36. Systems Cisco, "fec-summary-table," https://www.cisco.com/c/dam/en/us/products/se/2022/4/Collateral/fec-summary-table.pdf (2022). Accessed: 2025-05-13.
37. G. Caruso, I. N. Cano, D. Nesset, *et al.*, "Real-time 100 Gb/s PAM-4 for access links with up to 34 dB power budget," J. Lightwave Technol. **41**, 3491–3497 (2023).
38. A. Maharry, J. Liu, S. Misak, *et al.*, "First demonstration of an O-band coherent link for intra-data center applications," J. Lightwave Technol. **41**, 6643–6650 (2023).